remote sensing

Article

On-Orbit Radiometric Performance of GF-7 Satellite Multispectral Imagery

Hongzhao Tang [1,2], Junfeng Xie [2,*], Xinming Tang [2], Wei Chen [3] and Qi Li [1]

[1] School of Earth and Space Sciences, Peking University, Beijing 100871, China; tanghz@pku.edu.cn (H.T.); liqi@pku.edu.cn (Q.L.)
[2] Land Satellite Remote Sensing Application Center, Ministry of Natural Resources, Beijing 100094, China; tangxm@lasac.cn
[3] College of Geoscience and Surveying Engineering, China University of Mining and Technology, Beijing 100083, China; chenw@cumtb.edu.cn
* Correspondence: xiejf@lasac.cn; Tel.:+86-10-68412293

Abstract: China's first civilian, sub-meter, high-resolution stereo mapping satellite, GF-7, launched on 3 November 2019. Radiometric characterization of GF-7 multispectral imagery has been performed in this study. A relative radiometric accuracy evaluation of the GF-7 multispectral imagery was performed using several large uniform scenes, and the results showed that the accuracy is better than 2%. The absolute radiometric evaluation of the GF-7 satellite sensor was conducted at the Baotou and Dunhuang calibration sites, using the reflectance-based vicarious approach. The synchronous measurements of surface reflectance and atmospheric parameters were collected as the input for the radiative transfer model. The official radiometrically calibrated coefficient of the GF-7 multispectral imagery was evaluated with the predicted top-of-atmosphere (TOA) radiance from the radiative transfer model. The results indicated that the absolute radiometric accuracy of GF-7 multispectral imagery is better than 5%. In order to monitor the radiometric stability of the GF-7 satellite multispectral sensor, a relative and absolute radiometric accuracy assessment campaign should be performed several times a year.

Keywords: GF-7 satellite; radiometric performance; multispectral sensor; reflectance-based

check for updates

Citation: Tang, H.; Xie, J.; Tang, X.; Chen, W.; Li, Q. On-Orbit Radiometric Performance of GF-7 Satellite Multispectral Imagery. *Remote Sens.* **2022**, *14*, 886. https://doi.org/10.3390/rs14040886

Academic Editors: Mohammadmehdi Saberioon and Daniel Spengler

Received: 26 January 2022
Accepted: 10 February 2022
Published: 12 February 2022

1. Introduction

The Gao-Fen 7 (GF-7) satellite is China's first civilian, sub-meter, high-resolution stereo mapping satellite, and has the highest mapping accuracy standard of China's Gao-Fen series of satellites [1]. The GF-7 satellite was launched into orbit on 3 November 2019. The GF-7 satellite carried two optical cameras, which can obtain high-spatial-resolution optical stereo imagery pointing at forward and backward angles. The inclination angle of the forward-looking camera is +26° and the backward-looking camera is −5° from the nadir. The GF-7 satellite was designed to satisfy China's need for sub-meter, high-resolution satellite imageries, which were primarily used for 1:10,000 scale mapping. The GF-7 satellite can not only obtain accurate geometric information and structural information of ground features, but also multispectral information of features, when combined with the high-resolution multi-spectral camera, which plays a great role in China's natural resource and other industrial applications.

Most studies have focused on geometric calibration of the GF-7 satellite, and far less attention has been paid to radiometric calibration and validation [2]. Since the launch of the GF-7 satellite, GF-7 products have successfully played an important role in China's environmental, agricultural, and other quantitative applications, which require accurate and reliable radiometric information. The radiometric calibration accuracy of the GF-7 satellite is critical in these studies. The Land Satellite Remote Sensing Application Center (LASAC) of the Chinese Ministry of Natural Resources delivered the radiometrically corrected and georectified images (the standard level 1A products) of the GF-7 satellite to government and industry users. The radiometric calibration accuracy of the GF-7 satellite standard products must be evaluated.

The GF-7 satellite was designed to meet uniform relative radiometric responses across the scene. The pixel-to-pixel variation in the detector response of the GF-7 satellite sensor was eliminated by relative radiometric correction. LASAC performed a relative radiometric accuracy evaluation of the GF-7 imagery, using several large uniform scenes, such as a uniform ocean scene and the Libya invariant test site. The nonuniform variations in the GF-7 imagery could be detected in this study.

The absolute radiometric calibration of the GF-7 multispectral imagery is critical for providing highly accurate quantitative measurements of the Earth's surface. LASAC performed an absolute radiometric assessment of the GF-7 satellite sensor using the following two calibration sites: Dunhuang and Baotou. Reflectance-based vicarious radiometric calibration was commonly recognized as one of the most reliable approaches for on-orbit calibration and validation of an optical satellite sensor. Two independent absolute radiometric assessment campaigns of the GF-7 satellite, at different calibration sites, both used this reflectance-based approach. The surface reflectance and atmospheric parameters of the calibration sites were synchronously measured at the GF-7 satellite overpass time. These synchronous measurements were taken as the inputs of the radiative transfer model (such as MODTRAN 6.0), to predict the top-of-atmosphere (TOA) radiance, which was used to evaluate the GF-7 satellite sensor radiometric calibration. In order to ensure the accuracy and reliability of the GF-7 satellite multispectral imagery, the on-orbit radiometric performance must be regularly evaluated every year.

2. GF-7 Satellite Background

The GF-7 satellite is positioned on a 500 km sun-synchronous orbit, and covers the global region every 59 days. The designed life expectancy of this satellite is 5 years. It can survey the Earth at $\pm 84^\circ$ latitude, with a 5-day revisit time. Table 1 shows the technical specification of the GF-7 satellite. The GF-7 satellite carries two optical cameras (DLC) that point forward and backward, as shown in Figure 1. These two cameras are arranged at inclinations of $+26^\circ$ (forward-looking camera, FWD) and -5° (backward-looking camera, BWD) from the nadir. The FWD is a panchromatic camera, while the BWD is a multispectral imager with five bands, which include a panchromatic band and four multi-spectral bands (blue, green, red, and near infrared). The GF-7 DLC has about 20 km of ground swath. The GF-7 satellite is mainly used for mapping 1:10,000-scale topographic maps and geographic information products.

Table 1. The technical specification of the GF-7 satellite.

GF-7 Satellite	Technical Specification
Launch date	3 November 2019
Mission duration	5 Years
Orbit	500 km sun-synchronous orbit
Equator crossing time	10:30 AM
Repeat cycle time	59 days
Revisit cycle time	5 days
Spatial resolution of DLC	Panchromatic band: FWD: 0.80 m (GSD) BWD: 0.65 m (GSD) Multispectral band: BWD:2.60 m (GSD)
Swath width of DLC	20 km

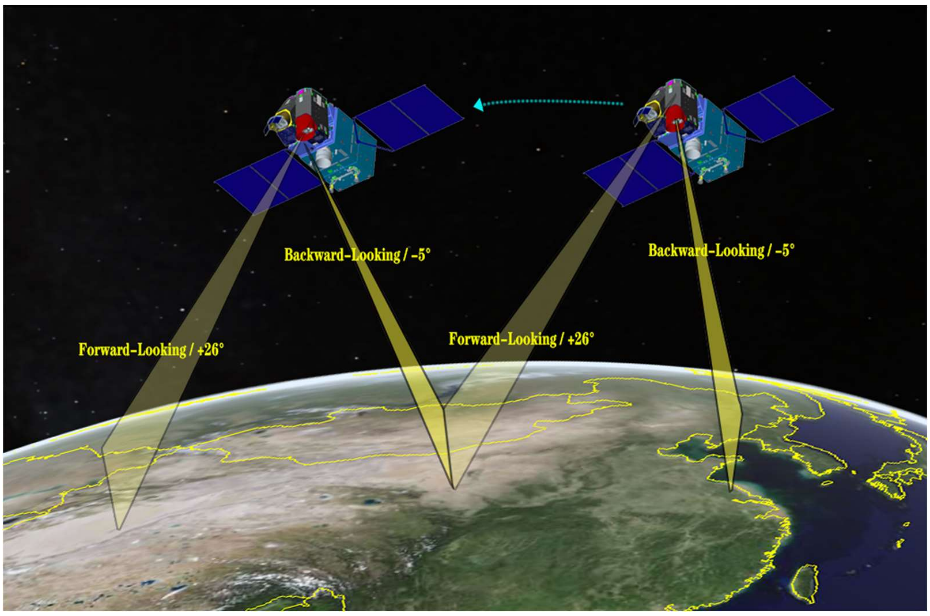

Figure 1. The DLC (forward-looking and backward-looking cameras) of the GF7 satellite.

2.1. GF-7 Multispectral Sensor

The GF-7 satellite carried two optical cameras (FWD and BWD), which can obtain high-spatial-resolution optical stereo imagery, pointing at forward and backward angles. The inclination angle of FWD is +26° and BWD is −5° from the nadir. The FWD is a panchromatic camera with a spatial resolution of 0.8 m, and the BWD is an imager that provides the repetitive acquisition of panchromatic (BWD-PAN, 450–920 nm) imagery with a spatial resolution of 0.65 m, and four-band multispectral imagery (BWD-MUX) of blue (460–530 nm), green (510–590 nm), red (620–690 nm), and near infrared (750–890 nm) with a spatial resolution of 2.6 m. Each camera has its own lens and consists of three single CCD lines located in an across-track dimension.

The spectral response function (SRF) of the GF-7 BWD is shown in Figure 2. Several of the spectral response properties of the GF-7 BWD are listed in Table 2.

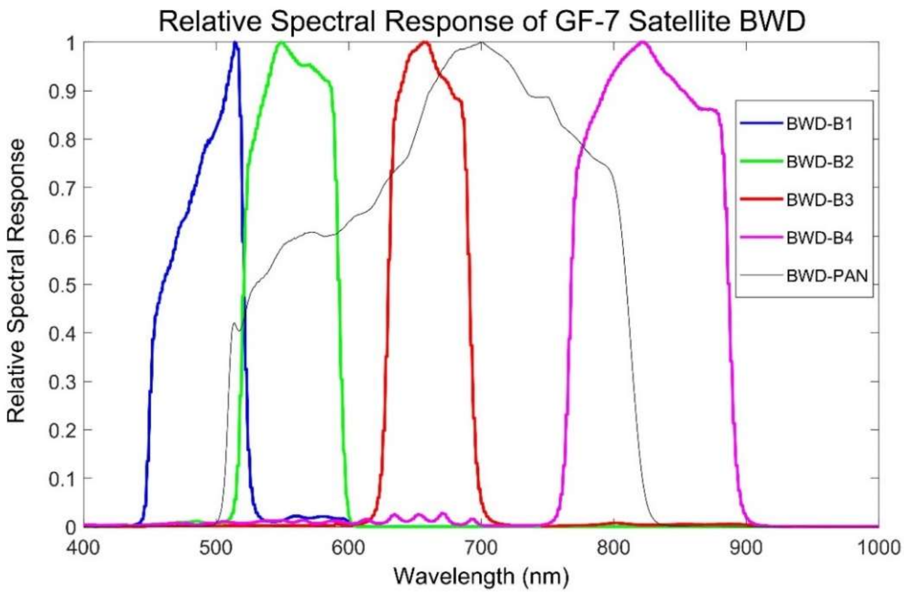

Figure 2. Normalized spectral response function of the GF-7 backward-looking camera.

Table 2. The spectral response properties of the GF-7 BWD.

Description	Band	Spectral Range (nm)	Center Wavelength (nm)	Specified Spectral Range at 50% Transmittance Points (nm)	Bandwidth (nm)
BWDPAN	PAN	450–920	746	556.2–912.5	470
BWDMUX	Blue	460–530	490	462.3–512.2	70
	Green	510–590	563	515.7–587.1	80
	Red	620–690	676	625.8–693.0	70
	NIR	750–890	807	763.9–885.4	140

2.2. LASAC GF-7 Data Products

Several types of GF-7 data products are delivered by LASAC to China's government and different industrial users. The standard level 1A products were both radiometrically and geometrically corrected (without using ground control points (GCPs)) and projected to a CGCS2000 datum. The standard level 1A products were orthorectified to improve the spatial accuracy with GCPs using Geomatica-PCI software [3]. In this study, all the radiometric analysis was performed on the standard level 1A products. The two cameras of the GF-7 satellite are formed by several time-delayed integral imaging (TDI) CCD linear arrays; the GF-7 imagery needs to be stitched in accordance with the geometric and radiometric characteristics. Evaluation and verification of the radiometric accuracy of the GF-7 imagery is essential for the application of satellite-retrieved data.

3. Relative Radiometric Accuracy Assessment

The GF-7 satellite BWD multispectral imager is a typical push-broom sensor, which consists of three single CCD arrays located in an across-track dimension. The linear detector array of the GF-7 BWD constructs an image one row at a time as the satellite moves [4,5]. Each CCD array of the BWD has 3072 detectors. There are two overlap regions between three CCD arrays, and each overlap region contains 108 detectors. Figure 3 shows the three CCD arrays of the GF-7 satellite multispectral sensor and the corresponding overlap region when imaging. Variations between the detectors of the GF-7 BWD always appear in the along-track scanning direction. Noise was apparent in the GF-7 satellite raw data before the relative radiometric correction. The radiometric nonuniformity always caused banding and striping, or dark lines, in the along-track scanning direction on the imagery [6–8]. The on-orbit detector-to-detector radiometric variation of the GF-7 multispectral imagery was corrected using relative radiometric calibration coefficients.

A relative radiometric accuracy evaluation of the GF-7 satellite multispectral imagery, using uniform scenes (such as desert and ocean), was performed in this study. Several large uniform scenes, including the Libya and Algeria pseudo-invariant calibration sites (PICs), have been used for evaluating the relative radiometric uniformity. The nonuniform variations in the GF-7 imagery could be detected using these large uniform scenes. Table 3 shows the worldwide uniform sites chosen for the relative radiometric accuracy assessment in this study.

Table 3. The uniform sites for relative radiometric accuracy assessment.

Num	Site	Latitude	Longitude	Area
1	Saharan	25.9° N	14.4° W	60 km × 60 km
2	Algeria	5.86° N	31.1° E	23 km × 20 km
3	Libya 4	28.52° N	23.39° E	23 km × 24 km

Figure 4 shows the GF-7 BWD-MUX blue band imagery of the uniform Libya 4 PICs. The columns of each detector (pixel) in the uniform imagery were summed and normalized. Figure 5 shows the mean normalized DN value curve of each detector in the uniform Libya 4 PICs on the GF-7 multispectral imagery, indicating that the relative differences in all the detectors are less than 2% for each band. We can observe that the array transitions between the different CCD arrays appear as step discontinuities in Figure 5. The largest relative difference appears in the array transition region. Similar results were obtained from the GF-7 multispectral imagery of the other larger uniform scenes in this study. The relative radiometric accuracy of the GF-7 multispectral imagery is better than 2% for all the bands.

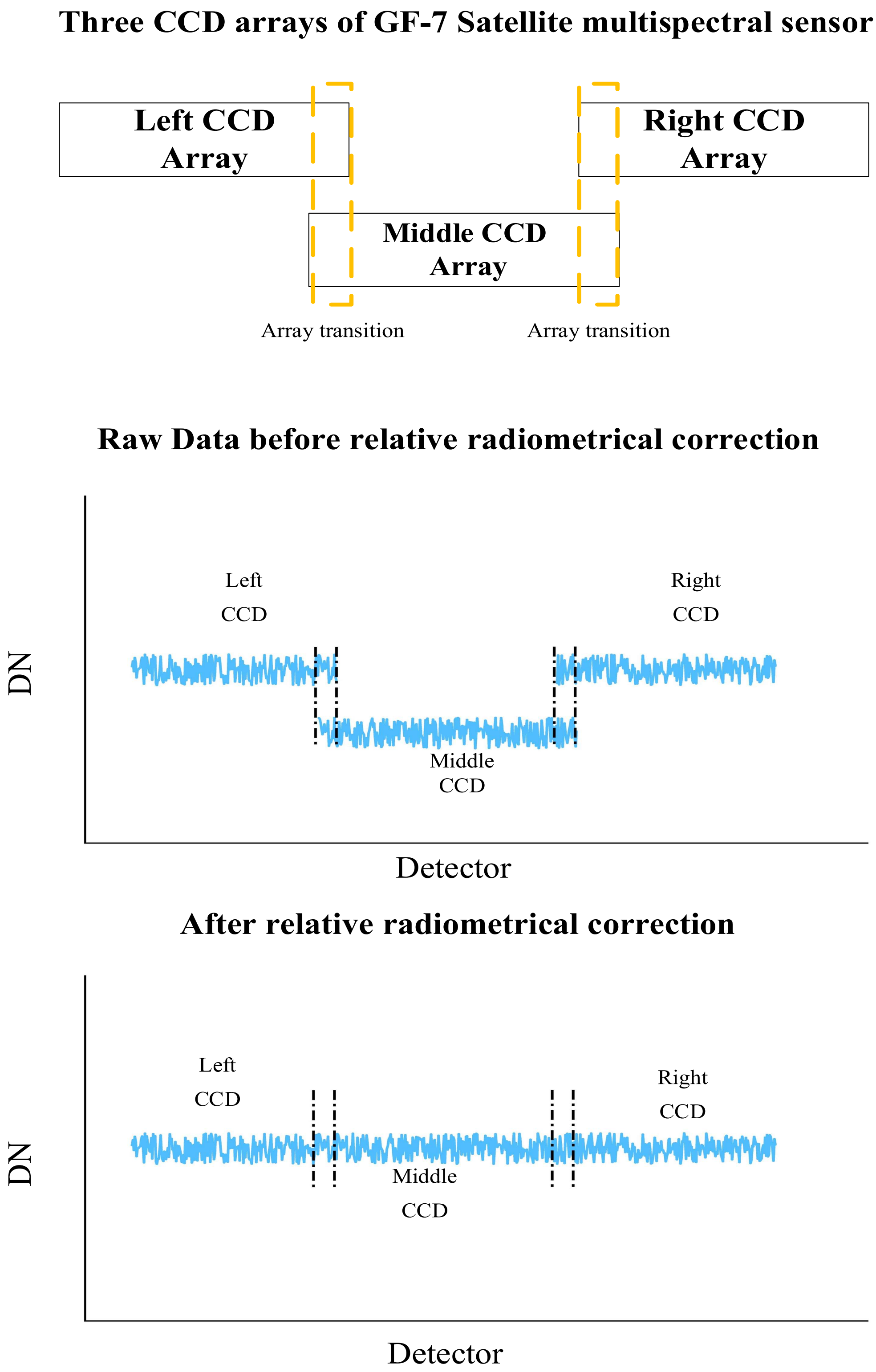

Figure 3. The three CCD arrays of the GF-7 satellite multispectral sensor.

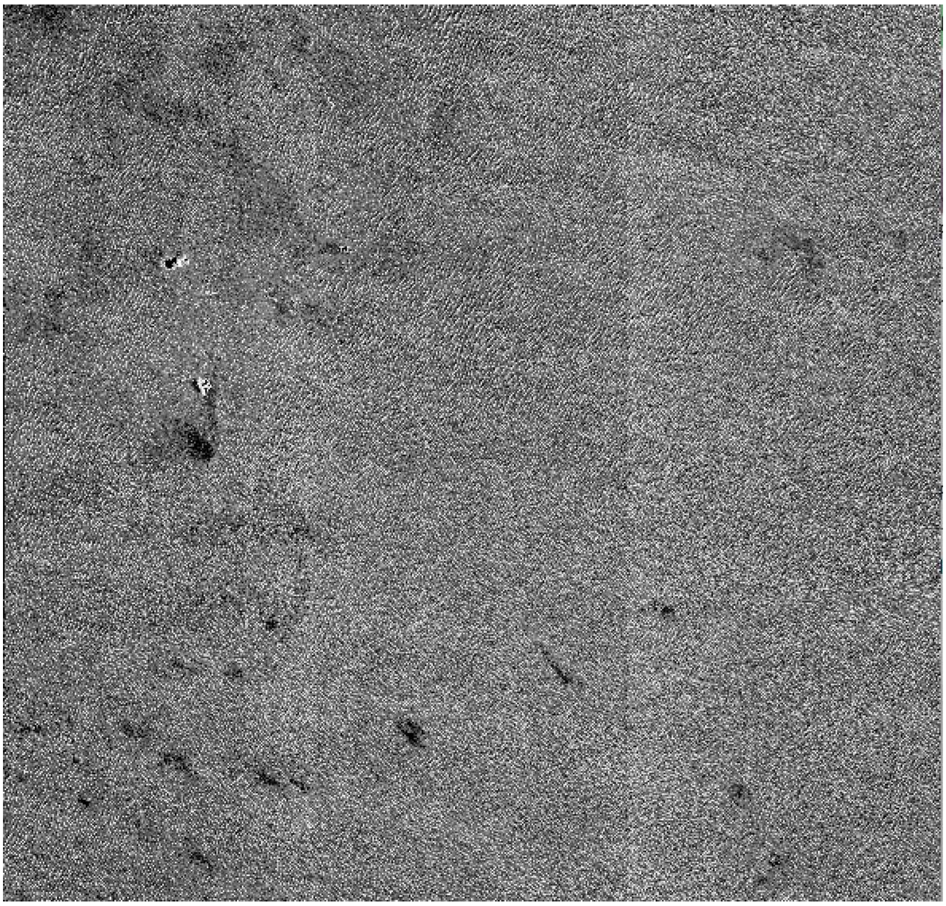

Figure 4. GF-7 BWD-MUX blue band imagery of the uniform Libya 4 PICs (8 August 2020).

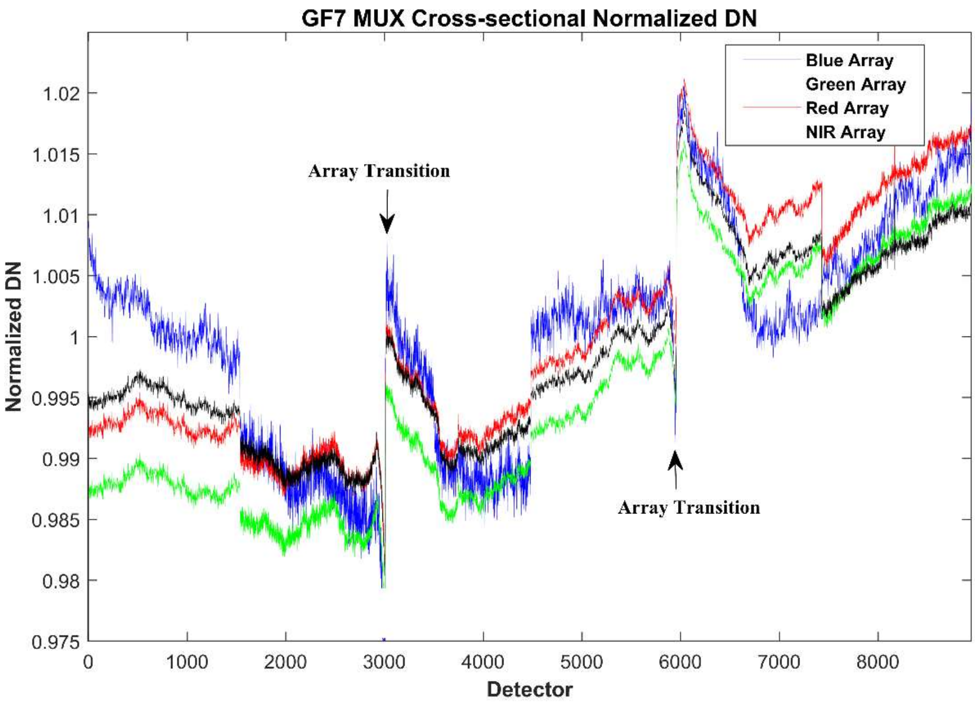

Figure 5. The normalized DN in the along-track direction of the uniform Libya 4 PICs.

4. Absolute Radiometric Accuracy Assessment

4.1. Reflectance-Based Radiometric Calibration Approach

Two independent absolute radiometric assessment campaigns of the GF-7 satellite at different calibration sites were performed by LASAC, using a reflectance-based approach. Reflectance-based radiometric calibration was commonly recognized as one of the most reliable approaches [9–12]. The surface spectral reflectance and atmospheric parameters of the calibration sites were synchronously measured during the GF-7 satellite overpass time. A radiative transfer model, such as MODTRAN, is commonly used for radiometric calibration and validation [13,14]. The predicted TOA radiance of the target was computed by MODTRAN using these synchronous measurements, and the sensor-measured TOA radiance was radiometrically calibrated from DN with absolute radiometric calibration coefficients. The relative difference between the predicted TOA radiance and sensor-measured TOA radiance was recognized as the accuracy of the radiometric calibration [15–19]. Figure 6 shows a detailed flow chart of the reflectance-based absolute radiometric evaluation approach.

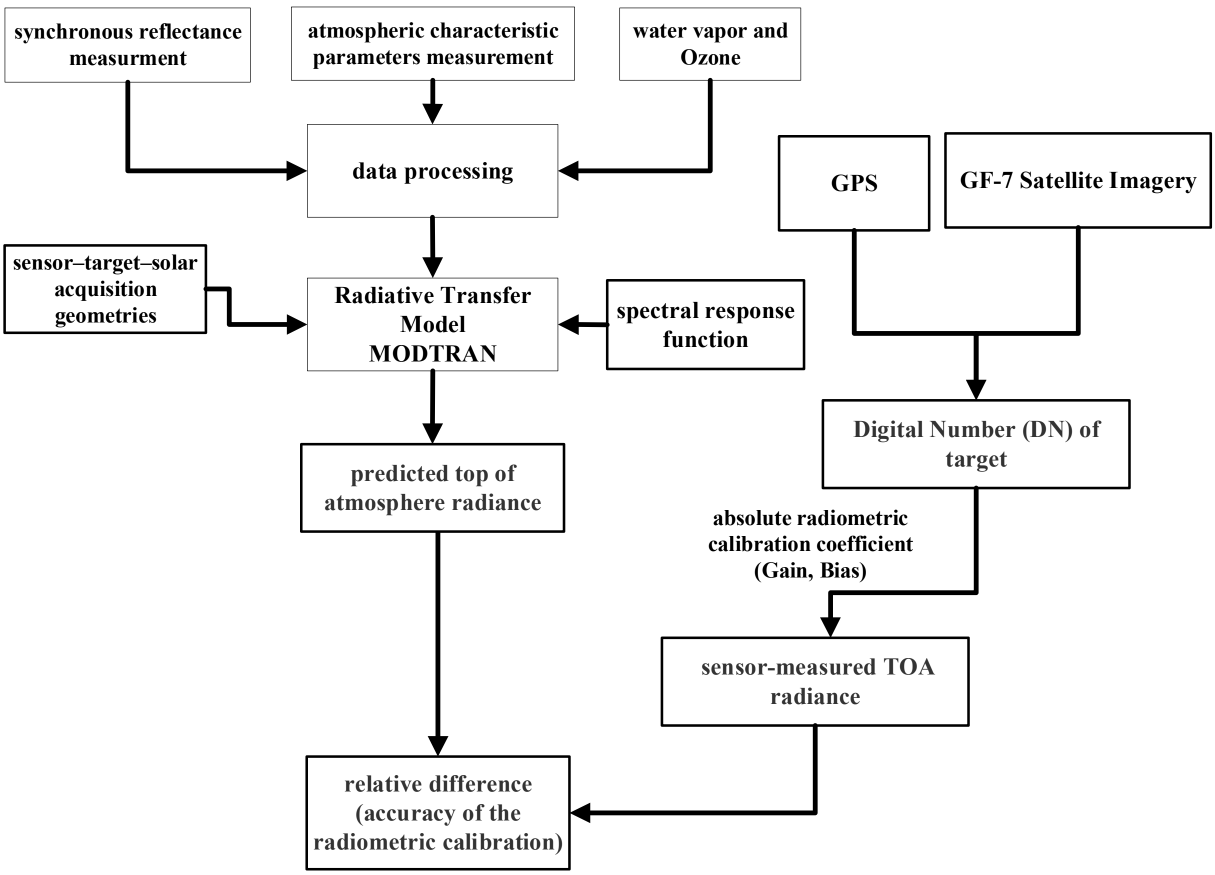

Figure 6. Detailed flow chart of the reflectance-based approach.

The TOA reflectance (known as apparent reflectance) of the GF-7 satellite multispectral imager $\rho^*(\mu_s, \phi_s; \mu_v, \phi_v)$ can be expressed as:

$$\rho^*(\mu_s, \mu_v, \phi_s - \phi_v) = \rho_a(\lambda) + \frac{\rho}{1 - S(\lambda)\rho} T_{\theta_s}(\lambda) T_{\theta_v}(\lambda) \quad (1)$$

The predicted TOA radiance $L_{predicted}(\theta_s, \phi_s; \theta_v, \phi_v)$ can be determined as follows:

$$L(\theta_s, \phi_s; \theta_v, \phi_v) = \frac{\mu_s E_s \rho^*}{\pi d^2} = \frac{\mu_s E_s}{\pi d^2} \left[\rho_a(\lambda) + \frac{\rho}{1 - S(\lambda)\rho} T_{\theta_s}(\lambda) T_{\theta_v}(\lambda) \right] \quad (2)$$

where θ_s is the solar zenith angle, θ_v is the viewing zenith angle, ϕ_s is the solar azimuth angle, and ϕ_v is the viewing azimuth angle. $\mu_s = \cos\theta_s$ and $\mu_v = \cos\theta_v$ are the cosine values. $T_{\theta_s}(\lambda)$ is the total transmittance from the solar to the Earth, and $T_{\theta_v}(\lambda)$ is the total transmittance from the Earth to the satellite sensor. $\rho_a(\lambda)$ is the atmospheric path reflectance, $S(\lambda)$ is the atmospheric spherical albedo, E_s is the exoatmospheric solar irradiance (ESUN), and d is the solar–Earth distance factor [20].

The average DN values of the targets were extracted from the GF-7 satellite multispectral imagery. The sensor-measured TOA radiance $L_{measured}$ was radiometrically calibrated from DN with absolute calibration coefficients.

$$L_{measured} = Gain \times DN + Bias \tag{3}$$

where $L_{measured}$ is the sensor-measured TOA radiance, expressed in units of $W \times m^{-2} \times sr^{-1} \times \mu m^{-1}$. $Gain$ and $Bias$ are the absolute radiometric calibration coefficients. DN is the digital number from the satellite imagery.

$\Delta L\%$ is the relative difference between the predicted TOA radiance and the sensor-measured TOA radiance, and this relative difference is recognized as the accuracy of the absolute radiometric calibration.

$$\Delta L\% = \frac{L_{measured} - L_{predicted}}{L_{predicted}} \times 100\% \tag{4}$$

4.2. Baotou Site Absolute Radiometric Calibration

4.2.1. Baotou Calibration Site

In 2013, the Committee on Earth Observation Satellites (CEOS) Working Group on Calibration and Validation (WGCV) Infrared and Visible Optical Sensors Subgroup (IVOS) established the radiometric calibration network (RadCalNet), which consists of four international calibration and validation sites located in the USA, France, Namibia, and China. The RadCalNet provides the automated in situ measurements of surface spectral reflectance, atmospheric parameters, and the corresponding nadir-viewing TOA reflectance using the radiative transfer model [21–23]. The Baotou site is located in the center of Inner Mongolia, China, and is currently operated by the Aerospace Information Research Institute, Chinese Academy of Science [24,25]. The Baotou site covers a flat area of 300 km^2, dominated by sand and bare soil. A series of targets and infrastructure have been built in the Baotou site to provide effective supports for the radiometric calibration and validation of high-resolution satellite optical sensors. Figure 7 shows the gray-scale permanent artificial targets in the Baotou site. The gray-scale permanent artificial targets are composed of four uniform gravel square targets (one black, one gray, and two white). The white, gray, and black targets, with known spectral reflectance [56%, 18% and 7%], have fairly flat spectral reflectance.

4.2.2. Surface Reflectance

The reflectance measurements of the targets were collected within about 30 min before and after the overpass time of the GF-7 satellite. The reflectance was measured by an SVC HR-1024i spectroradiometer, which covered the wavelength range from 350 nm to 2500 nm. SVC HR-1024i is a high-resolution, field-portable spectroradiometer, and the spectral resolution in the 400–1000 nm wavelength range is 1.5 nm. The reflectance measurement was interpolated at 1 nm intervals in the 350–2500 nm wavelength range by the SVC software. The size of each gray-scale permanent artificial target is 48 m × 48 m; it covers about 15 cross-track pixels and 15 along-track pixels of the GF-7 multispectral imagery. We took 3 × 3 pixels as one sample, and 25 samples were collected in each single target. The parameters of the SVC spectroradiometer were configured to measure five spectra per sample, and then a total of 100 samples and more than 500 spectra were collected. Figure 8 shows the averaged reflectance measurement from the gray-scale permanent artificial targets in the range of 400–1000 nm.

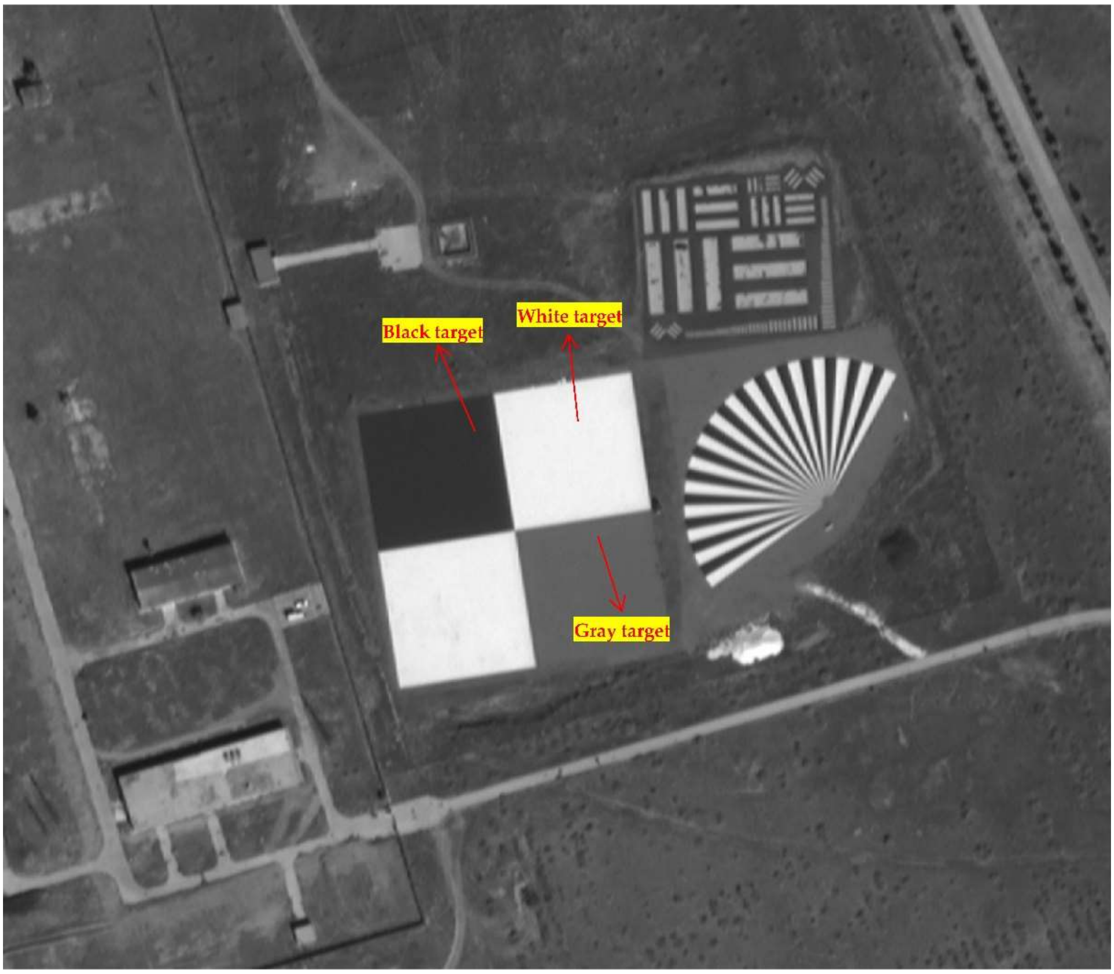

Figure 7. The gray-scale permanent artificial targets at the Baotou site of GF-7 BWD imagery (15 September 2020).

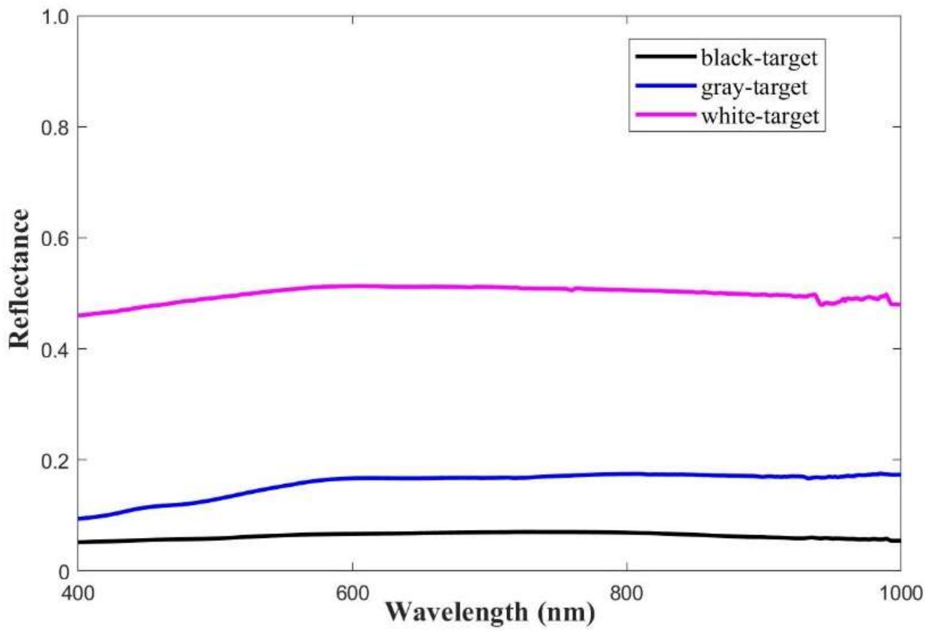

Figure 8. Spectral reflectance measurement data of gray-scale permanent targets.

In this study, a multi-angle bidirectional reflectance distribution function (BRDF) measurement instrument was used to quantify the bidirectional reflectance effect of the gray-scale permanent targets, as shown in Figure 9. The BRDF characteristics of the gray-scale permanent targets were measured according to the angle of incidence and reflection, using the SVC spectroradiometer with the multi-angle instrument [26]. The measured BRDF values of the targets were interpolated at 1 nm intervals in the 400–1000 nm wavelength range.

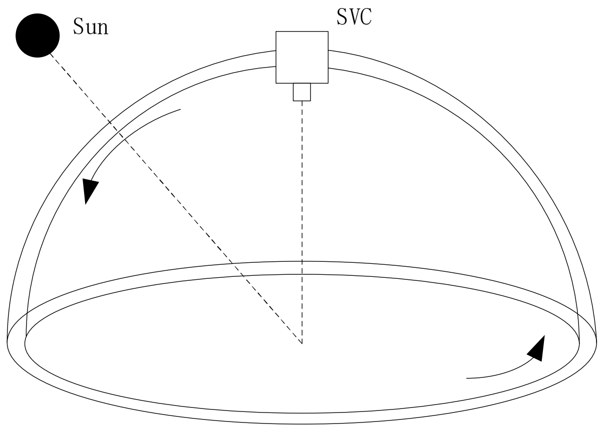

Figure 9. The BRDF measurement instrument.

The anisotropy factor (ANIF) was used to interpret the BRDF effects of elevation and azimuth direction in this study [27,28].

$$\mathrm{ANIF}(\theta_\mathrm{i}, \varphi_\mathrm{i}, \theta_\mathrm{v}, \varphi_\mathrm{v}, \lambda) = \frac{\mathrm{BRDF}(\theta_\mathrm{i}, \varphi_\mathrm{i}, \theta_\mathrm{v}, \varphi_\mathrm{v}, \lambda)}{\mathrm{BRDF}_N(\theta_\mathrm{i}, \varphi_\mathrm{i}, \theta_\mathrm{N}, \varphi_\mathrm{v}, \lambda)} \quad (5)$$

where $\mathrm{BRDF}(\theta_\mathrm{i}, \varphi_\mathrm{i}, \theta_\mathrm{v}, \varphi_\mathrm{v}, \lambda)$ is the BRDF for the reflected radiance in the azimuth (φ_v) and zenith (θ_v) directions at wavelength (λ), which comes from the incident radiance in the azimuth (φ_i) and zenith (θ_i) directions. $\mathrm{BRDF}_N(\theta_\mathrm{i}, \varphi_\mathrm{i}, \theta_\mathrm{N}, \varphi_\mathrm{v}, \lambda)$ is measured in the nadir direction ($\theta_\mathrm{N} = 0^\circ$). Figure 10 shows the ANIF values of the gray target from the BRDF measurement.

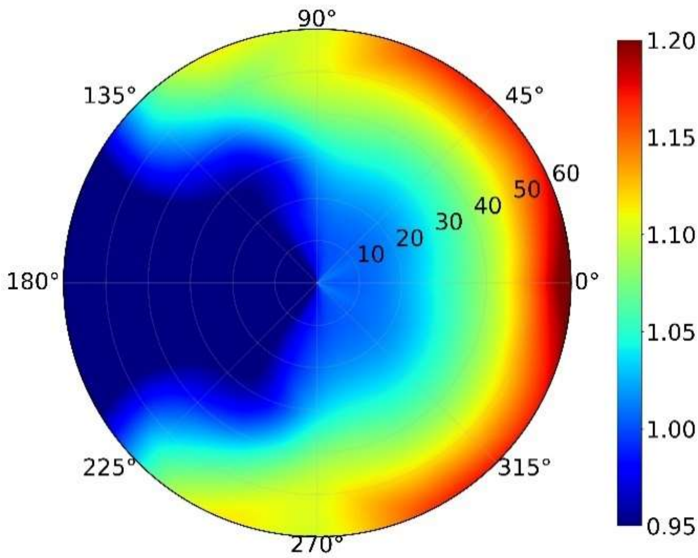

Figure 10. The ANIF values of gray target from BRDF measurement.

These ANIF values are used to better understand the BRDF effects of the gray-scale permanent targets for the GF-7 radiometric calibration. The SVC reflectance measurement in the nadir direction $\rho(\theta_i, \varphi_i, \theta_N, \varphi_v, \lambda)$ of the gray-scale permanent targets was modified by Formula (6), where $\rho^*(\theta_i, \varphi_i, \theta_v, \varphi_v, \lambda)$ is the reflectance of the GF-7 for the relative sensor–target–solar geometry condition [29].

$$\rho^*(\theta_i, \varphi_i, \theta_v, \varphi_v, \lambda) = \frac{\rho(\theta_i, \varphi_i, \theta_N, \varphi_v, \lambda)}{\mathrm{ANIF}(\theta_i, \varphi_i, \theta_v, \varphi_v, \lambda)} \quad (6)$$

4.2.3. Atmospheric Measurements

The atmospheric parameters at the Baotou site were measured by a Cimel CE318 sun photometer. The aerosol optical depth (AOD), aerosol microphysical information, and column amounts of water vapor can be collected automatically every day at this site. Figure 11 shows the synchronous measurement of aerosol optical depth at the Baotou site during the overpass of the GF-7 satellite on 23 July 2020. These atmospheric parameter measurements serve as inputs in MODTRAN, to predict the TOA radiance.

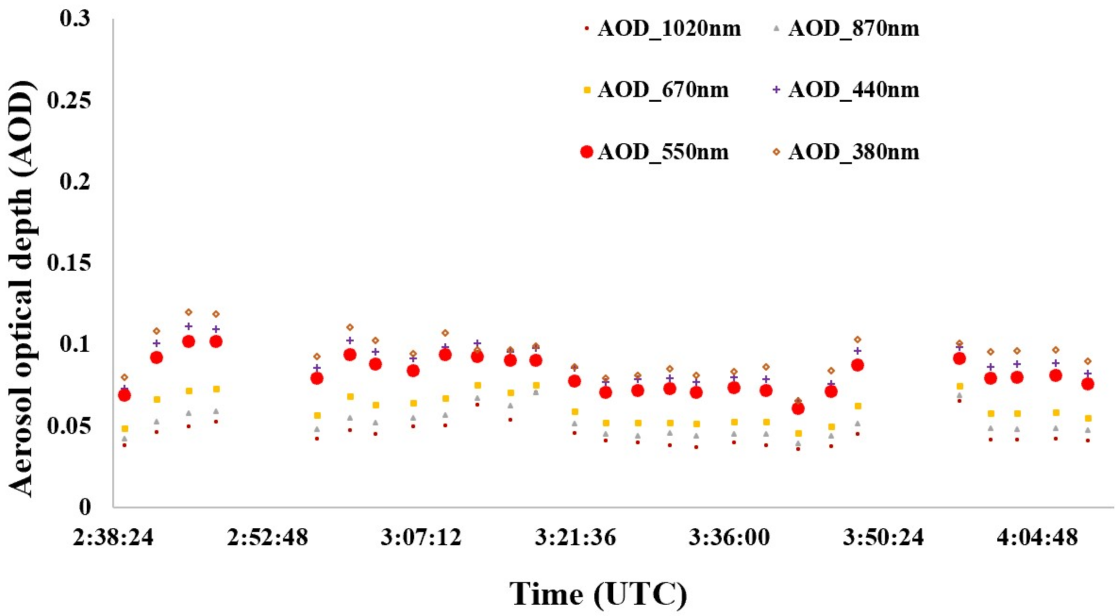

Figure 11. Synchronous measurement of the atmospheric parameters of the Baotou site on 23 July 2020.

4.2.4. Reflectance-Based Radiometric Calibration Campaign

Vicarious reflectance-based radiometric calibration and evaluation campaigns were performed at the Baotou site on the following four separate days: 23 July, 28 July, 15 September, and 20 September 2020. There was no cloud cover on any of the days. Table 4 shows the solar–target–satellite acquisition geometric conditions of the GF7 satellite at the Baotou site. The GF-7 satellite acquired imagery on 23 June at 03:46 (UTC time) at a viewing elevation angle of 84.484° and a viewing azimuth angle of 177.117°, as shown in Figure 12. The viewing elevation angles of the other three imageries acquired on 28 July, 15 September, and 20 September are all more than 82°. Tables 5 and 6 summarize the absolute radiometric calibration result of the GF-7 satellite at the Baotou site on 23 and 28 July, and 15 and 20 September 2020. The comparison between the sensor-measured TOA radiance and the predicted TOA radiance in Tables 5 and 6 showed that the relative difference is less than 5% for all the bands of the GF-7 multispectral imagery, indicating that the accuracy of the absolute radiometric calibration is better than 5%.

Table 4. Solar–target–satellite acquisition geometric conditions of the GF7 satellite at the Baotou site.

Date	Overpass Time (UTC)	Solar Elevation (°)	Viewing Elevation (°)	Solar Azimuth (°)	Viewing Azimuth (°)
23 July 2020	03:46:26	65.412	84.484	143.097	177.117
28 July 2020	03:44:57	64.285	82.554	143.641	146.680
15 September 2020	03:48:11	50.564	84.614	160.732	191.945
20 September 2020	03:47:13	48.724	83.789	161.678	160.266

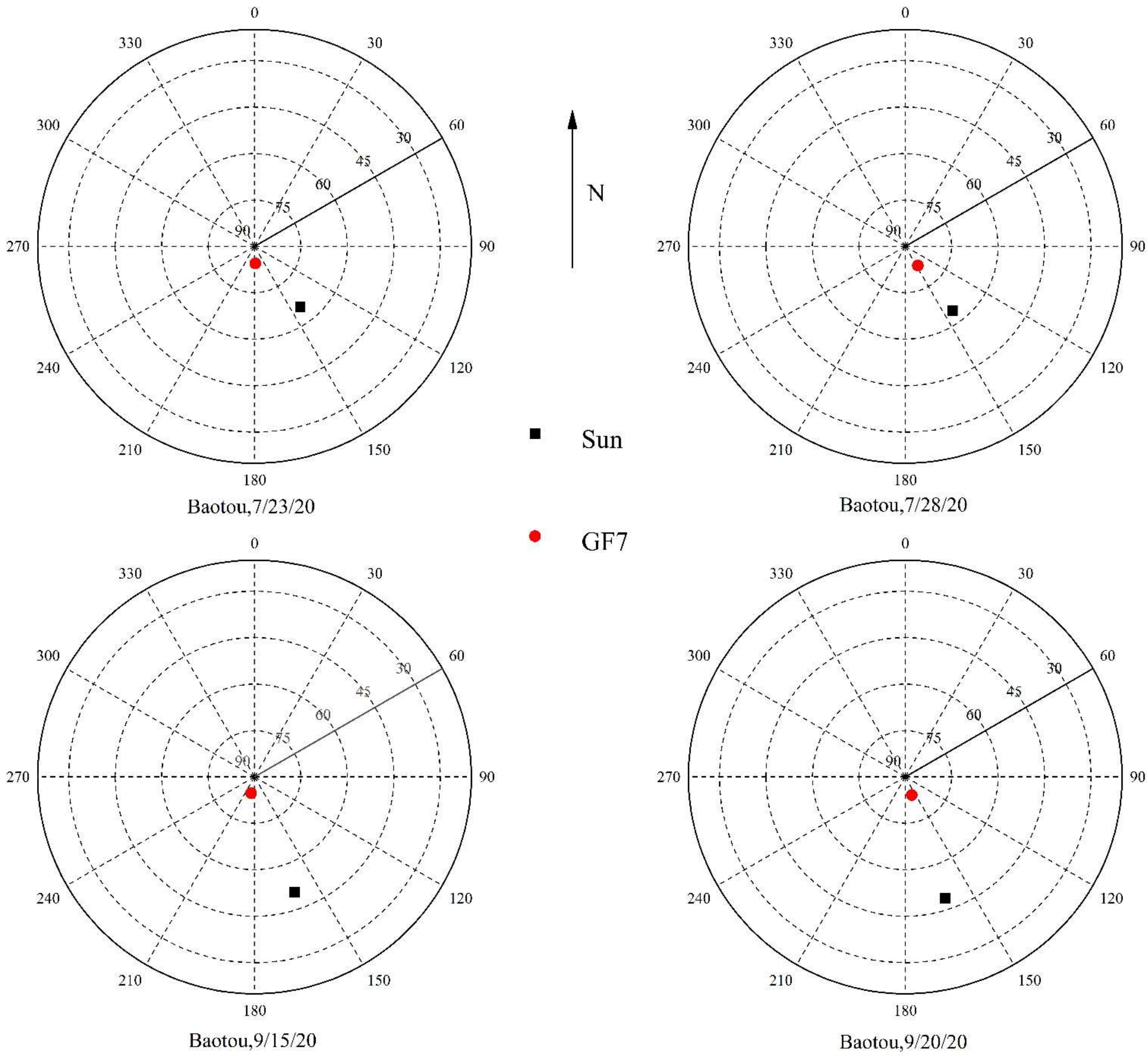

Figure 12. The GF-7 satellite Baotou site acquisition geometry.

Table 5. The absolute radiometric calibration result of the GF-7 satellite at the Baotou site on 23 and 28 July 2020.

Date	Band	Target	$L_{measured}$ ($W \times m^{-2} \times sr^{-1} \times \mu m^{-1}$)	$L_{predicted}$ ($W \times m^{-2} \times sr^{-1} \times \mu m^{-1}$)	$\Delta L\%$
23 July 2020	Blue	Black	58.588	56.472	3.61%
		Gray	90.581	87.675	3.21%
		White	233.324	221.986	4.86%
	Green	Black	45.366	43.142	4.90%
		Gray	85.648	82.794	3.33%
		White	211.256	217.673	−3.04%
	Red	Black	34.575	35.878	−3.77%
		Gray	72.852	75.672	−3.87%
		White	180.602	188.231	−4.22%
	NIR	Black	21.524	22.004	−2.23%
		Gray	51.116	53.168	−4.01%
		White	124.943	127.552	−2.09%
28 July 2020	Blue	Black	58.002	55.789	3.97%
		Gray	89.675	86.614	3.53%
		White	230.734	219.766	4.99%
	Green	Black	44.912	43.051	4.32%
		Gray	84.792	81.792	3.67%
		White	209.143	215.039	−2.74%
	Red	Black	34.229	35.444	−3.43%
		Gray	72.123	74.756	−3.52%
		White	178.796	185.953	−3.85%
	NIR	Black	21.309	21.738	−1.97%
		Gray	50.605	52.525	−3.66%
		White	123.694	126.009	−1.84%

Table 6. The absolute radiometric calibration result of the GF-7 satellite at the Baotou site on 15 and 20 September 2020.

Date	Band	Target	$L_{measured}$ ($W \times m^{-2} \times sr^{-1} \times \mu m^{-1}$)	$L_{predicted}$ ($W \times m^{-2} \times sr^{-1} \times \mu m^{-1}$)	$\Delta L\%$
15 September 2020	Blue	Black	50.438	51.879	−2.78%
		Gray	76.954	79.030	−2.63%
		White	179.236	185.092	−3.16%
	Green	Black	40.598	39.558	2.63%
		Gray	70.735	73.713	−4.04%
		White	165.577	160.149	3.39%
	Red	Black	30.954	29.991	3.21%
		Gray	65.673	62.680	4.78%
		White	138.312	134.854	2.56%
	NIR	Black	19.338	18.627	3.82%
		Gray	45.292	44.029	2.87%
		White	98.884	94.357	4.80%

Table 6. *Cont.*

Date	Band	Target	$L_{measured}$ ($W \times m^{-2} \times sr^{-1} \times \mu m^{-1}$)	$L_{predicted}$ ($W \times m^{-2} \times sr^{-1} \times \mu m^{-1}$)	$\Delta L\%$
20 September 2020	Blue	Black	49.934	51.251	−2.57%
		Gray	76.184	78.074	−2.42%
		White	177.444	182.852	−2.96%
	Green	Black	40.192	39.079	2.85%
		Gray	70.028	72.821	−3.84%
		White	163.921	158.211	3.61%
	Red	Black	30.644	29.628	3.43%
		Gray	65.016	62.040	4.80%
		White	136.929	133.222	2.78%
	NIR	Black	19.145	18.402	4.04%
		Gray	44.839	43.496	3.09%
		White	97.895	93.394	4.82%

4.3. Dunhuang Site Absolute Radiometric Calibration

The Dunhuang site was China's national radiometric calibration site, which has been used to calibrate China's satellites (such as the Feng-Yun series, Zi-Yuan series, and Gao-Fen series of satellites) since the 1990s. The Dunhuang site was selected as one of the "instrumented sites" (LandNet) by CEOS WGCV [30,31]. The Gobi Desert at the Dunhuang calibration site is large, spatially uniform, and homogeneous. The spectral reflectance of the Gobi Desert is stable, with an annual variation of less than 2%. Figure 13 shows the Gobi Desert at the Dunhuang site.

Figure 13. The Dunhuang calibration site.

The Dunhuang site is located about 25 km west of Dunhuang city, Gansu Province, China. The central region of the Gobi Desert is located at the coordinates 94.41° E, 40.09° N, with an elevation of 1280 m above sea level. The size of the central region is 1000 m × 1000 m; it covers more than 360 cross-track pixels and 360 along-track pixels of the GF-7 multispectral imagery.

The methodology took 30 × 30 pixels as one sample, and more than 150 samples were collected in the central region of the Gobi Desert and more than 600 spectra were collected at the Dunhuang calibration site. Figure 14 shows the average and standard deviations of the surface reflectance measurement of the Gobi Desert in the range of 400–1000 nm. Since the Gobi Desert is stable and homogeneous, the standard deviation of more than 600 spectra is less than 1%, as shown in Figure 14. The atmospheric parameters at the Dunhuang site were measured by a Cimel CE318 sun photometer. The daily AOD at 550 nm varied from 0.11 to 0.18 during the campaigns at the Dunhuang test site, and the synchronous AOD measurements at the GF-7 satellite overpass time were less than 0.15.

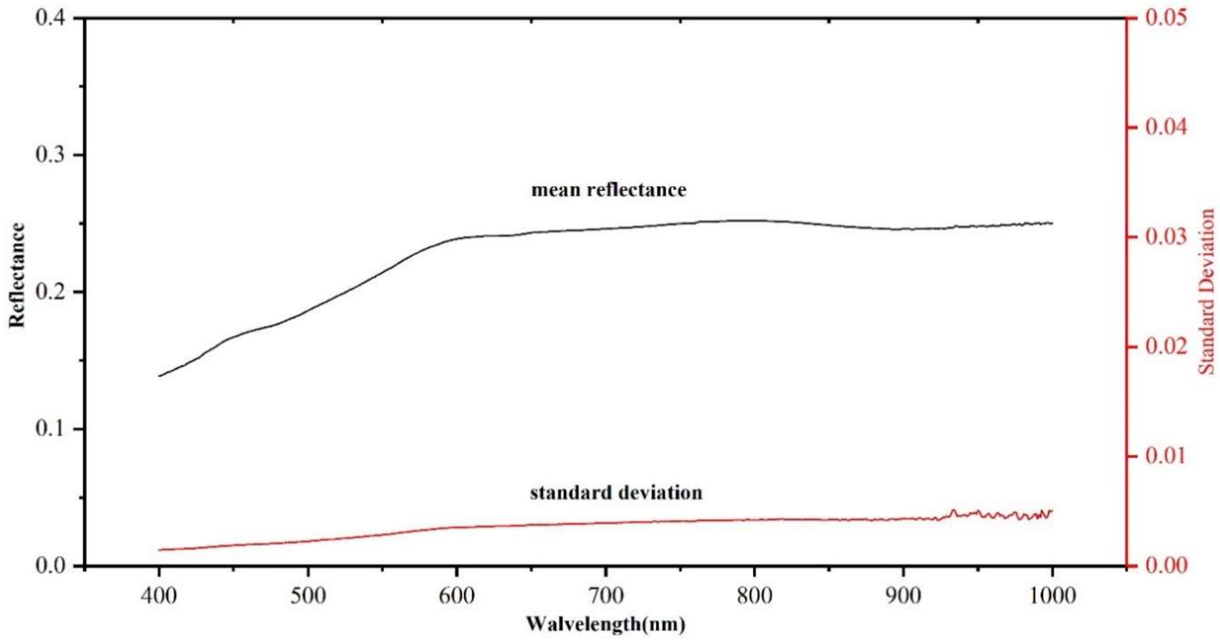

Figure 14. Surface reflectance and standard deviation of the Gobi Desert at the Dunhuang test site.

The BRDF effect of the Gobi Desert at the Dunhuang test site was also measured by the multi-angle measurement instrument, which was exactly the same as described in Section 4.2.

The vicarious radiometric calibration campaign was performed at the Dunhuang test site on the following two separate days: 10 July and 25 July 2020. There was also no cloud cover on either day. Table 7 shows the solar–target–satellite acquisition geometric conditions of the GF7 satellite at the Dunhuang test site. The GF-7 satellite acquired imagery on 10 June at 03:46 (UTC time) at a viewing elevation angle of 84.622° and a viewing azimuth angle of 187.648°, as shown in Figure 15. The other imagery was acquired on 25 July 2020 at a viewing elevation angle of 77.835° and a azimuth angle of 126.181°, as shown in Figure 15. The viewing elevation angle of the other imagery acquired on 25 July was less than 80°. Table 8 summarizes the absolute radiometric calibration result of the GF-7 satellite at the Dunhuang test site on 10 July and 25 July 2020. The comparisons between the measured TOA radiance and the predicted TOA radiance in Table 8 showed the relative differences on July 10 for the blue band (4.43%), green band (2.02%), red band (1.17%), and NIR band (2.22%), as well as the relative differences on 25 July for the blue band (4.68%), green band (3.88%), red band (3.78%), and NIR band (3.26%), which were less than 5% in all the bands. The calibration results of the Dunhuang site agreed well with the results at the Baotou site.

Table 7. Solar–target–satellite acquisition geometric conditions of the GF7 satellite at the Dunhuang site.

Date	Overpass Time (UTC)	Solar Elevation (°)	Viewing Elevation (°)	Solar Azimuth (°)	Viewing Azimuth (°)
10 July 2020	04:47:03	67.835	84.622	139.761	187.648
25 July 2020	04:42:11	65.128	77.835	140.366	126.181

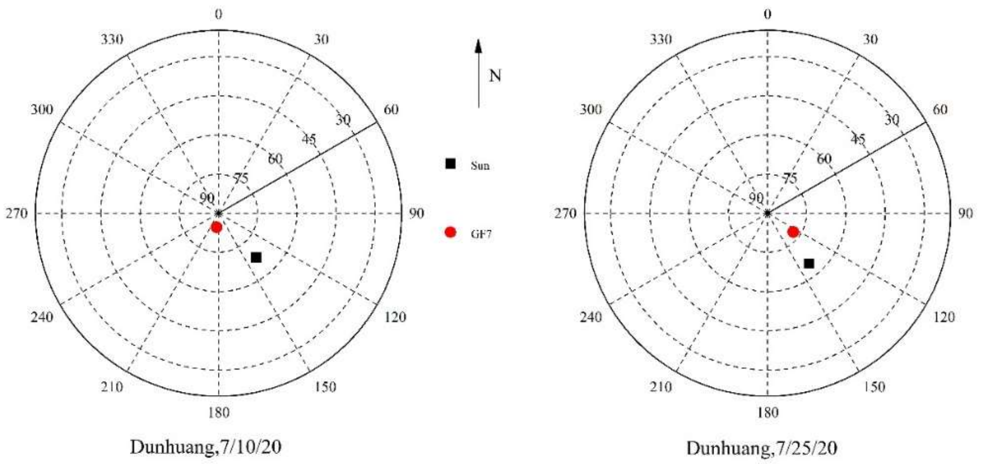

Figure 15. The GF-7 satellite Dunhuang test site acquisition geometry.

Table 8. The absolute radiometric calibration result of the GF-7 satellite at the Baotou site.

Date	Band	Target	$L_{measured}$	$L_{predicted}$	$\Delta L\%$
			$W \times m^{-2} \times sr^{-1} \times \mu m^{-1}$		
10 July 2020	Blue	Gobi	75.490	72.143	4.43%
	Green	Gobi	82.732	81.060	2.02%
	Red	Gobi	88.205	87.171	1.17%
	NIR	Gobi	72.180	70.580	2.22%
25 July 2020	Blue	Gobi	76.399	72.822	4.68%
	Green	Gobi	86.290	82.945	3.88%
	Red	Gobi	90.273	86.861	3.78%
	NIR	Gobi	73.906	71.499	3.26%

5. Conclusions

The relative and absolute radiometric accuracy of GF-7 satellite imagery is critical for the quantitative applications of natural resources, environment, agriculture, and other industries. In this study, a relative radiometric accuracy evaluation of GF-7 multispectral imagery, using several uniform scenes (such as the uniform Libya, Algeria, and Saharan pseudo-invariant calibration test sites), was performed by LASAC. Nonuniform variations in the original GF-7 imagery were detected before relative radiometric calibration, and the relative radiometric accuracy of the GF-7 multispectral imagery is better than 2% in these large uniform scenes. The evaluation of the absolute radiometric accuracy of the GF-7 satellite sensor at Baotou and Dunhuang, two different calibration sites, was performed by a reflectance-based approach. The BRDF of the targets was measured by a multi-angle instrument with an SVC spectroradiometer. The synchronous measurement of the surface spectral reflectance was modified by the surface BRDF model, and the atmospheric parameters were coupled with the exoatmospheric solar irradiance spectrum and relative spectral response of the sensor as inputs in MODTRAN, to predict the TOA radiance. The predicted TOA radiance was compared with the sensor-measured TOA radiance to evaluate the absolute radiometric accuracy of the GF-7 multispectral imagery. The two independent absolute radiometric assessment campaigns of the GF-7 satellite at the Baotou and Dunhuang sites were performed by LASAC. The radiometrically calibrated accuracy of the GF-7 multispectral imagery was evaluated using different targets at two different calibration sites. The results at the two calibration sites showed that the absolute radiometric accuracy is better than 5%. Considering the results shown in this study, the relative and absolute radiometric accuracy assessment campaign should be performed several times a year, to monitor the radiometric stability of the GF-7 satellite multispectral sensor. This study can also supply a reference to the on-orbit radiometric performance of Chinese high-resolution satellites.

Author Contributions: H.T. developed the research plan and supervised the work, J.X., X.T., W.C. and Q.L. participated in the literature review, method selection, data acquisition and discussions. All authors have read and agreed to the published version of the manuscript.

Funding: This work was supported by the National Key R&D Program of China, 2018YFB0504800, 2018YFB0504801.

Institutional Review Board Statement: Not applicable.

Informed Consent Statement: Not applicable.

Conflicts of Interest: The authors declare no conflict of interest.

References

1. Cao, H.Y.; Liu, F.Q.; Zhao, C.G.; Dai, J. The study of high resolution stereo mapping satellite. *Natl. Remote Sens. Bull.* **2021**, *25*, 1400–1410.
2. Xie, J.; Liu, R.; Zhao, C.G.; Tang, H.Z.; Dou, X.H.; Yang, C.; Xi, S. Design and Data Processing of China's First Spaceborne Laser Altimeter System for Earth Observation: GaoFen-7. *IEEE J. Sel. Top. Appl. Earth Obs. Remote Sens.* **2020**, *13*, 1034–1044. [CrossRef]
3. Cheng, P.; Chaapel, C. WorldView-2 Pansharpening and Geometric Correction. *GeoInformatics Mag.* **2010**, *6*, 1–6.
4. Pagnutti, M.; Ryan, R.E.; Kelly, M.; Holekamp, K.; Zanoni, V.; Thome, K. Radiometric characterization of IKONOS multispectral imagery. *Remote Sens. Environ.* **2003**, *88*, 53–68. [CrossRef]
5. Henderson, B.G.; Krause, K.S. Relative radiometric correction of QuickBird imagery using the side-slither technique on orbit. *Proc. SPIE -Int. Soc. Opt. Eng.* **2004**, *5542*, 1–12.
6. Ron, M.; Julia, B.; Raviv, L.; Brian, M.; Esad, M.; Lawrence, O.; Pat, S.; Kelly, V. Landsat-8 Operational Land Imager (OLI) Radiometric Performance On-Orbit. *Remote Sens.* **2015**, *7*, 2208–2237.
7. Markham, B.; Barsi, J.; Kvaran, G.; Kaita, E.; Ong, L.; Haque, M.O.; Mishra, N.; Czaplamyers, J.; Pahlevan, N.; Helder, D. Landsat-8 Operational Land Imager Radiometric Calibration and Stability. *Remote Sens.* **2014**, *6*, 12275–12308. [CrossRef]
8. Pesta, F.; Bhatta, S.; Helder, D. Radiometric Non-Uniformity Characterization and Correction of Landsat 8 OLI Using Earth Imagery-Based Techniques. *Remote Sens.* **2015**, *7*, 430–446. [CrossRef]
9. Thome, K.J. Absolute Radiometric Calibration of Landsat 7 ETM+ Using the Reflectance-Based Method. *Remote Sens. Environ.* **2001**, *78*, 27–38. [CrossRef]
10. Czapla-Myers, J.; McCorkel, J.; Anderson, N.; Thome, K.; Biggar, S.; Helder, D.; Aaron, D.; Leigh, L.; Mishra, N. The Ground-Based Absolute Radiometric Calibration of Landsat 8 OLI. *Remote Sens.* **2014**, *7*, 600–626. [CrossRef]
11. Biggar, S.F.; Dinguirard, M.C.; Gellman, D.I.; Henry, P.J.; Jackson, R.D.; Moran, M.S.; Slater, P.N.; Guenther, B.W. Radiometric Calibration of SPOT 2 HRV-a Comparison of Three Methods. *Proc. SPIE* **1991**, *1493*, 155–162.
12. Dinguirard, M.; Slater, P.N. Calibration of Space-Multispectral Imaging Sensors: A Review. *Remote Sens. Environ.* **1999**, *68*, 194–205. [CrossRef]
13. Gao, H.L.; Gu, X.F.; Tao, Y. The Research Overview on Visible and Near-infrared Channels Radiometric Calibration of Space-borne Optical Remote Sensors. *Remote Sens. Inf.* **2010**, *4*, 12.
14. Xiong, X.; Barnes, W.; Xie, X.; Salomonson, V. On-orbit performance of Aqua MODIS on-board calibrators. *Proc. SPIE* **2005**, *5978*, 75–80.
15. Ponzoni, F.J.; Junior, J.Z.; Lamparelli, R. In-flight absolute calibration of the CBERS-2 CCD sensor data. *An. Da Acad. Bras. De Ciências* **2008**, *80*, 799–804. [CrossRef]
16. Naughton, D. Absolute radiometric calibration of the RapidEye multispectral imager using the reflectance-based vicarious calibration method. *J. Appl. Remote Sens.* **2011**, *5*, 3544. [CrossRef]
17. Hu, X.; Liu, J.; Sun, L.; Rong, Z.G.; Li, Y.; Zhang, Y.; Zheng, Z.; Wu, R.; Zhang, L.; Gu, X.F. Characterization of CRCS Dunhuang test site and vicarious calibration utilization for Fengyun (FY) series sensors. *Can. J. Remote Sens.* **2010**, *36*, 566–582. [CrossRef]
18. Pinto, T.; Ponzoni, F.; Ruy, C.; Larry, L.; Nischal, M.; David, A.; Helder, D. First in-Flight Radiometric Calibration of MUX and WFI on-Board CBERS-4. *Remote Sens.* **2016**, *8*, 405. [CrossRef]

19. Markham, B.; Thome, K.J.; Barsi, J.A.; Kaita, E.; Helder, D.L.; Barker, J.L.; Scaramuzza, P.L. Landsat-7 ETM+ on-orbit reflective-band radiometric stability and absolute calibration. *IEEE Trans. Geosci. Remote Sens.* **2004**, *42*, 2810–2820. [CrossRef]
20. Chen, W.; Yan, L.; Li, Z.; Xiong, X.X. In-flight absolute calibration of an airborne wide-view multispectral imager using a reflectance-based method and its validation. *Int. J. Remote Sens.* **2013**, *34*, 1995–2005. [CrossRef]
21. Bouvet, M.; Thome, K.; Berthelot, B.; Bialek, A.; Czapla-Myers, J.; Fox, N.P.; Goryl, P.; Henry, P.; Ma, L.; Marcq, S.; et al. RadCalNet: A Radiometric Calibration Network for Earth Observing Imagers Operating in the Visible to Shortwave Infrared Spectral Range. *Remote Sens.* **2019**, *11*, 2401. [CrossRef]
22. Liu, Y.K.; Ma, L.L.; Qiu, S.; Qian, Y.G.; Li, C.R. On-orbit radiometric calibration of the optical sensors on-board SuperView-1 satellite using three independent methods. *Opt. Express* **2020**, *28*, 8.
23. Liu, Y.K.; Ma, L.L.; Wang, N.; Qian, Y.G.; Li, C.R. Vicarious radiometric calibration/validation of Landsat-8 operational land imager using a ground reflected radiance-based approach with Baotou site in China. *J. Appl. Remote Sens.* **2017**, *11*, 1.
24. Li, C.R.; Ma, L.L.; Tang, L.L.; Gao, C.X.; Qian, Y.G.; Wang, N.; Wang, X.H. A comprehensive calibration site for high resolution remote sensors dedicated to quantitative remote sensing and its applications. *Natl. Remote Sens. Bull.* **2021**, *25*, 198–219.
25. Li, C.R.; Ma, L.L.; Gao, C.X.; Tang, L.L.; Liu, Y.K. Permanent target for optical payload performance and data quality assessment: Spectral characterization and a case study for calibration. *J. Appl. Remote Sens.* **2014**, *8*, 083498. [CrossRef]
26. Feingersh, T.; Dorigo, W.; Richter, R.; Dor, E.B. A new model-driven correction factor for BRDF effects in HRS data. In Proceedings of the 4th EARSeL Workshop on Imaging Spectroscopy, Warsaw, Poland, 26–29 April 2005; Volume 4, pp. 565–576.
27. Kim, J.; Jin, C.; Choi, C.; Ahn, H. Radiometric characterization and validation for the KOMPSAT-3 sensor. *Remote Sens. Lett.* **2015**, *6*, 529–538. [CrossRef]
28. Jong-Min, Y.; Jisoo, H.; Jae-Heon, J.; Kwon-Ho, L.; Chang-Suk, L. Initial Radiometric Characteristics of KOMPSAT-3A Multispectral Imagery Using the 6S Radiative Transfer Model, Well-Known Radiometric Tarps, and MFRSR Measurements. *Remote Sens.* **2017**, *9*, 130.
29. Jin, C.; Ahn, H.; Seo, D.; Choi, C. Radiometric Calibration and Uncertainty Analysis of KOMPSAT-3A Using the Reflectance-Based Method. *Sensors* **2020**, *20*, 2564. [CrossRef]
30. Badawi, M.; Helder, D.; Leigh, L.M.; Jing, X. Methods for Earth-Observing Satellite Surface Reflectance Validation. *Remote Sens.* **2019**, *11*, 1543. [CrossRef]
31. Jing, X.; Leigh, L.M.; Pinto, T.; Helder, D. Evaluation of RadCalNet Output Data Using Landsat 7, Landsat 8, Sentinel 2A, and Sentinel 2B Sensors. *Remote Sens.* **2019**, *11*, 541. [CrossRef]